2015

Acoustic emission monitoring of wind turbine blades

Jeremy Van Dam
Iowa State University

Leonard J. Bond
Iowa State University, bondlj@iastate.edu

Acoustic emission monitoring of wind turbine blades

Abstract
Damage to wind turbine blades can, if left uncorrected, evolve into catastrophic failures resulting in high costs and significant losses for the operator. Detection of damage, especially in real time, has the potential to mitigate the losses associated with such catastrophic failure. To address this need various forms of online monitoring are being investigated, including acoustic emission detection. In this paper, pencil lead breaks are used as a standard reference source and tests are performed on unidirectional glass-fiber-reinforced-polymer plates. The mechanical pencil break is used to simulate an acoustic emission (AE) that generates elastic waves in the plate. Piezoelectric sensors and a data acquisition system are used to detect and record the signals. The expected dispersion curves generated for Lamb waves in plates are calculated, and the Gabor wavelet transform is used to provide dispersion curves based on experimental data. AE sources using an aluminum plate are used as a reference case for the experimental system and data processing validation. The analysis of the composite material provides information concerning the wave speed, modes, and attenuation of the waveform, which can be used to estimate maximum AE event – receiver separation, in a particular geometry and materials combination. The foundational data provided in this paper help to guide improvements in online structural health monitoring of wind turbine blades using acoustic emission.

Disciplines
Structures and Materials

Comments
This paper is from *Proc. SPIE* 9439, Smart Materials and Nondestructive Evaluation for Energy Systems 2015, 94390C (March 27, 2015); doi:10.1117/12.2084527. Posted with permission.

Acoustic emission monitoring of wind turbine blades

Jeremy Van Dam*[a], Leonard J. Bond[a]
[a]Center for Nondestructive Evaluation, Iowa State University, 1915 Scholl Road, 111 ASC II, Ames, IA, USA 50011-3041

ABSTRACT

Damage to wind turbine blades can, if left uncorrected, evolve into catastrophic failures resulting in high costs and significant losses for the operator. Detection of damage, especially in real time, has the potential to mitigate the losses associated with such catastrophic failure. To address this need various forms of online monitoring are being investigated, including acoustic emission detection. In this paper, pencil lead breaks are used as a standard reference source and tests are performed on unidirectional glass-fiber-reinforced-polymer plates. The mechanical pencil break is used to simulate an acoustic emission (AE) that generates elastic waves in the plate. Piezoelectric sensors and a data acquisition system are used to detect and record the signals. The expected dispersion curves generated for Lamb waves in plates are calculated, and the Gabor wavelet transform is used to provide dispersion curves based on experimental data. AE sources using an aluminum plate are used as a reference case for the experimental system and data processing validation. The analysis of the composite material provides information concerning the wave speed, modes, and attenuation of the waveform, which can be used to estimate maximum AE event – receiver separation, in a particular geometry and materials combination. The foundational data provided in this paper help to guide improvements in online structural health monitoring of wind turbine blades using acoustic emission.

Keywords: Composites, glass-fiber-reinforced-polymer, acoustic emission, Lamb waves, dispersion curves, online health monitoring

1. INTRODUCTION

Wind energy growth has triggered a need for inspecting and monitoring technologies to guide maintenance for wind turbines, which, in many cases, are located on remote and hard to reach sites, especially when considering offshore applications. Such sites, prescribe a need for a remote online structural health monitoring (OSHM) system that gives data, which, ideally, can enable the reduction of the costs associated with operations and maintenance (O&M). The wind turbine blades (WTB) specifically require OSHM to ensure constant operation and reduction in the potential for critical failures that can arise from the growth of what is initially minor damage. As WTBs grow in length, operators are seeking to mitigate losses that occur from unscheduled downtime and critical WTB failures. Based on GCube Insurance data, WTBs accounted for 41.4% of damage claims with an average cost of $240,000 and a maximum of about $700,000[1]. OSHM has the ability to drive down costs by detecting damage before replacement is necessary and limiting unscheduled maintenance events. The current methods of scheduled maintenance and run-to-failure do not provide adequate damage detection and consistent and quality monitoring.

Over the last decade, wind energy has relied on the production tax credit (PTC) to ensure economic profitability, which is shown in the correlation between installation rates and the PTC renewal. Increasing revenue and reducing expenses will push wind energy into economic freedom from political and policy uncertainties. For this reason, the wind industry is pursuing technologies to increase revenue by increasing per-turbine output, i.e. build taller towers, use longer blades and utilize better generators. As size-limitations emerge for the height of towers, length of blades and power rating of each turbine, and full-scale operation experience matures, wind plant owners and operators are increasingly recognizing the importance and potential economic benefits of O&M cost reductions. There is however, a reluctance in the wind energy industry to reduce O&M costs by installing both CBM and OSHM systems because of the added initial and installation costs. O&M costs make up approximately 20% of the levelized cost of wind turbines, which is significant, but that also means 80% of the expenses, $1,630/kW, are related to repayment of capital costs[2]. Any increase in the costs of installation is therefore undesirable from the perspective of wind plant operators, which implies any added OSHM system must be seen to be cost effective, in terms of the return on investment provided.

*jrmyvndm@iastate.edu; phone 1-515-294-8152; fax 1-515-294-7771; www.cnde.iastate.edu

Smart Materials and Nondestructive Evaluation for Energy Systems 2015, edited by Norbert G. Meyendorf,
Proc. of SPIE Vol. 9439, 94390C · © 2015 SPIE · CCC code: 0277-786X/15/$18 · doi: 10.1117/12.2084527

After increasing revenue, the second action by the wind industry, although lower in terms of its economic impact on profitability, is the reduction of expenses. Condition based maintenance technologies are starting to emerge and be deployed for the gearbox, bearings, generator, and blades[3]. Ensuring a higher capacity factor (reduced downtime and increased percentage of time when in operation and generating) not only decreases O&M costs as a percentage of total costs in relation to income, but also maintains revenue from continuous electricity generation. With the increasingly available data on O&M costs and component failure rates, cost benefit analysis studies have increased in accuracy and are now able to identify areas of potential cost reductions. Several studies have shown that SHM can reduce the levelized cost of wind energy by reducing O&M costs and unscheduled downtimes[4,5,6]. Providing the health status of a component allows for timely and efficient maintenance and potentially repairs and replacements during periods of low wind. Operating until failure may also cause added costs from the cascading effects where one component failure causes another to fail, and these effects result in extended downtimes, due, for example, to additional replacement component delivery times and the occurrence of an appropriate weather window for repair and replacement activities.

An ideal OSHM system is accurate, reliable, inexpensive, robust, and sensitive. An inexpensive system requires lower additional capital costs added to the project, and the costs should be potentially recoverable from a small number of defect events in a wind farm. Secondly, the system must be robust, because wind turbines operate in extreme and remote environments with broad temperature ranges. Thunderstorms are common in areas ideal for wind plants, resulting in increased chances of lightning strikes. Systems placed within the WTB must endure the forces resulting from various rotational speeds and fluctuating wind loads exerted on the WTB in addition to the environmental effects. Lastly, the OSHM system must be sensitive and accurate, giving a low number of false calls or missed calls. Effective event detection, defect characterization and localization, allows for the implementation of the appropriate maintenance strategies. A system capable of signaling the defect location and the degree of severity provides a basis for the determination of intervention needed, estimation of remaining useful life, and optimization of the life for a damaged or failing component.

An emerging method for monitoring composite structures is with acoustic emission (AE) detection. AE has been used for decades in fatigue experiments to determine and monitor blade condition during destructive testing[7], and field-testing is emerging[8]. Sensors using piezoelectric elements and optical fibers can detect elastic waves travelling in the material, which result from changes in the micro and macro structure of the material. Impacts and damage formation (e.g., cracks, delaminations, fiber breaks etc.) are examples of structural changes that cause elastic wave generation events, called acoustic emissions. The AE signals can give data that indicate the health of the structure by comparing current conditions to standard operating conditions via changes in the signal parameters, frequency spectrum and different wave modes. When compared to the ideal system, AE detection offers the benefits of low cost, robustness, and sensitivity. The principle downside of an AE system is the relatively low signal to noise ratio and the issues of acoustic and electrical background "noise", which limit the ability of the system to accurately and reliably characterize and locate the damage occurring during operation.

To use AE as an SHM tool, there is a need for improvements in signal identification, especially in a complex structure like a WTB. Understanding the source and elastic wave characteristics in the material are the first steps to refining signal analysis and defect identification. This paper will begin by examining WTB structures and materials and will then consider acoustic wave propagation. A state-of-the-art evaluation identifies the key needs and limitations for AE SHM in WTBs. This paper reports an investigation of AE generated wave detection and propagation in the glass-fiber reinforced polymer (GFRP) material used in WTBs, which includes the determination of wave speeds and attenuation rates. Aluminum plate samples are used to provide experimental system and data processing validation. The analysis also includes the examination of the Gabor wavelet transform, and its ability to identify wave modes and frequency dependent wave propagation characteristics. The culmination of this work will contribute to the progress of incorporating AE sensors into WTBs for the use of OSHM.

2. EXPERIMENTAL PROCEDURE

2.1 Wind turbine blade structure

As WTBs grow in length, operators are seeking to mitigate losses that occur from unscheduled downtime and critical WTB failures. The current commercial standard WTB is between 40m and 90m in length, but Vestas, Alstom, and Seimens have begun to offer WTBs exceeding 100m in length. To achieve longer lengths and maintain economic viability, the design must balance aerodynamics, structural strength, material properties, and capital costs. Aerodynamic efficiency primarily dictates the shape, but the structural strength, material properties, and capital costs determine the internal structure and the

materials used. An internal box structure combines with various materials to provide a WTB that can sustain the wind and mass loads, while ensuring economic viability for the wind turbine.

Figure 1 shows the cross section of a 9-meter Sandia National Laboratory CX-100 WTB. The left side is the leading edge; the right side is the trailing edge, and in the center on the top and bottom is the spar cap. The WTB shown in figure 1 contains a single shear web that provides structural stiffness and strength; most commercial WTBs contain a box spar structure. The section in which the shear web attaches to the top and bottom is termed the spar cap. The primary forms of assembling the blade include pre-impregnation (pre-preg) and injection molding. During the pre-preg process, the composite material is semi-cured and stored until the mold is ready, after which it is fully cured. Injection molding occurs when the glass or carbon fiber is enclosed in a bag and the resin is injected. A vacuum pulls the resin across the reinforcement layers to ensure mixing[9]. WTB manufacturing typically consists of constructing the top, bottom, and shear web separately and then bonding the three components with an epoxy glue[10].

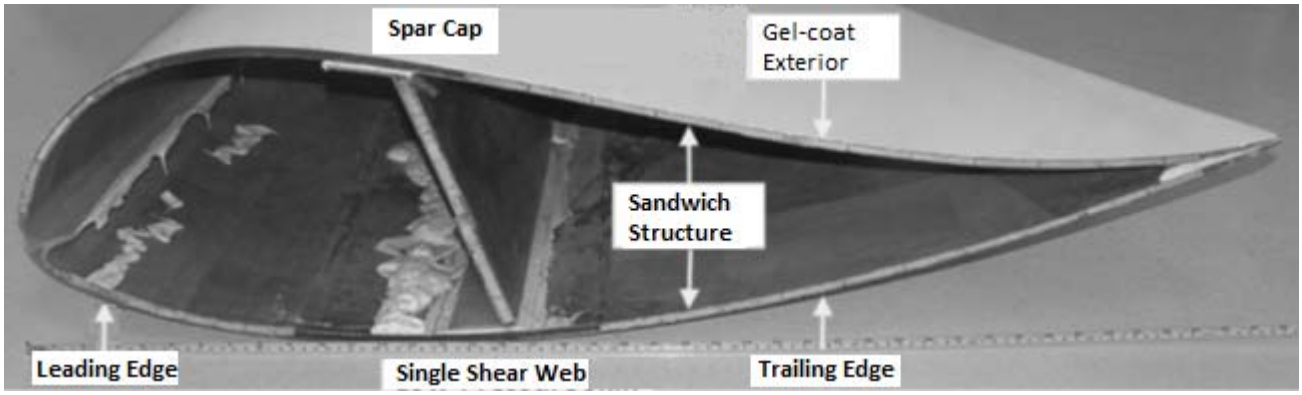

Figure 1. The cross-section of Sandia National Laboratory's CX-100 WTB.

(a) (b)

Figure 2. Examples of parts of a WTB showing (a) the sandwich structure leading up to the trailing edge and (b) the complete GFRP spar cap connected to wooden shear webs, which are 5 cm thick.

The shell consists of three sections, the leading edge, the trailing edge, and the spar cap. Figure 2 shows the tip of the trailing edge (a) and the spar cap (b). A two-part epoxy paste[11] bonds the top shell to the bottom shell along the leading and trailing edges, and connects the shear webs to the spar cap, as shown in figures 1 and 2. Residual epoxy paste shown in the figures reveals the low precision methods used to bond the components together. The leading and trailing edges of the shell incorporate a sandwich structure by having thin layers of fiber reinforcement enclose a core material, but the entire spar section consists of the fiber reinforcement. The sandwich structure (fiber-reinforcement/core/fiber-reinforcement) in the leading and trailing edges makes use of the fiber and core material properties to provide high strength and stiffness and yet give low weight to the WTB. Figure 2(b) shows the spar cap connected to two shear webs, in contrast to the single shear web design shown in figure 1. The shear webs bond to the spar cap using the same two-part epoxy paste as the leading and trailing edges, and are typically made from a GFRP/balsa wood sandwich structure. In commercial WTBs, a gel coat will cover the exterior to provide protection, specifically from precipitation and humidity.

WTBs consist of three primary materials, reinforcement, resin, and core. The most common form of reinforcement is glass fiber, specifically E-Glass, but H-Glass is increasing in use due to it having a higher stiffness than E-Glass. Use of carbon fiber, which has exceptional stiffness, fluctuates due to concerns over cost and issues regarding handling. The fibers bond together using a resin or epoxy. Polyesters with low cycle times and costs and epoxies with excellent mechanical properties are primarily used, but vinyl esters are increasing in use due to a good tradeoff between material properties, cost, and cycle time. The core materials primarily used are PVC and balsa wood. PVC has material properties superior to balsa wood but at a higher cost. Despite the lower cost, balsa wood has concerns regarding consistency in its properties and high resin absorption. PET and Tycor, custom-engineered core materials, are increasing in use and are becoming commercially mature. Compared to balsa wood, PET has a lower cost and improved material consistency, and Tycor has a reduced resin uptake.

2.2 Acoustic emission sources

An impact event, from debris or bird strikes, can cause delaminations and cracks in the resin, greatly reducing the structural health of the composite structure. Even low velocity impacts can cause damage that may propagate into critical failures[12]. Early detection provides the opportunity to repair or replace sections with minor damage before damage growth. Thus, detection and localization of such events is important for an OSHM system. To test the system various methods are used to create an AE source including ultrasonic transducers, ball impacts, glass capillary fractures, and pencil-lead breaks (PLB). Ultrasonic transducers provide the ability to input a precise signal, but calibration of the transducer is necessary. Ball impacts, glass capillary fracture, and PLBs provide step function disturbances that consist of a broad band of frequencies. Normalizing the varying detected amplitudes allows for comparative measurements[13]. PLBs were chosen as the source of AE for these experiments.

The Hsu-Nielsen[14] pencil-lead break test, first proposed by Nelson Hsu in 1977[15], is an established acoustic emission reference source. Pressing and breaking the pencil-lead against the material surface creates an elastic wave that provides a signal containing a wideband of frequencies and the flexural and extensional wave modes. The lead length, its diameter, and the angle of the lead relative to the surface affect the elastic waves generated and consequently the detected signal[16]. Because of the wide use of the PLB test, the American Society for Testing and Materials (ASTM) created a PLB standard, E976-10[17]. Comparisons between PLB tests allow for the assessment of the sensors and AE detection system.

A PLB event creates a waveform containing both flexural and extensional modes, but the orientation and angle in which the lead broke determines the amplitude of each mode[18], as shown in figure 3. In-plane displacements, breaking the lead on the side of the sample, causes larger amplitude extensional modes; out-of-plane displacements, breaking the lead on the top surface, causes larger amplitude flexural modes. During active monitoring, the amplitude ratio of one mode to the other can help characterize the source of the AE.

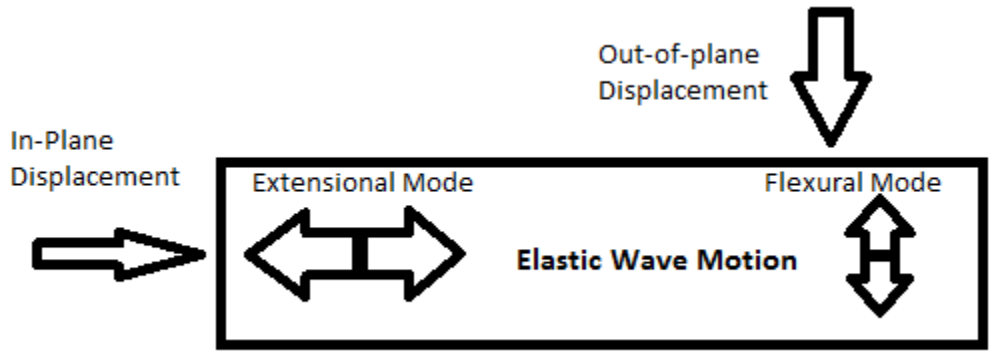

Figure 3. Schematic showing wave the motion resulting from in-plane and out-of-plane source displacements.

Figure 4 shows the recorded signal from the two types of PLBs, out-of-plane displacement, figure 4(a), and in-plane displacement, figure 4(b). The solid box in each plot of figure 4 outlines the flexural wave, and the dashed box outlines the extensional wave, which is faster than the flexural wave causing it to arrive first in each case. The out-of-plane displacement creates a small extensional wave followed by a larger flexural wave, and the in-plane displacement creates a large amplitude extensional wave followed by a smaller amplitude flexural wave. Due to the speed variation of the

modes, a larger separation distance between the source and the sensors will result in a longer separation of the two wave modes.

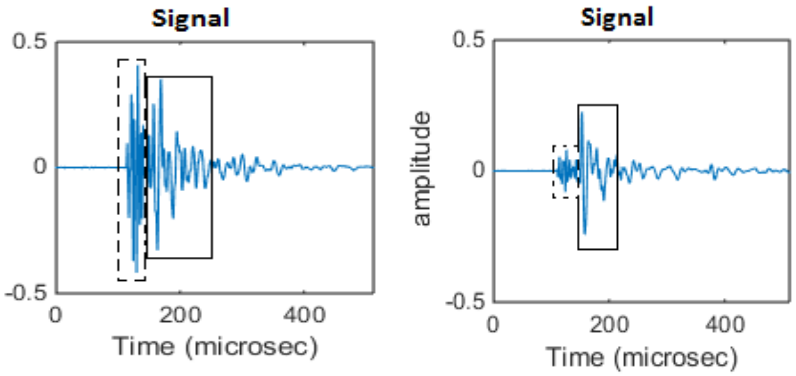

(a) (b)

Figure 4. Example of signals from PLB source measured at 5 cm (a) in-plane displacement and (b) out-of-plane displacement.

2.3 State-of-the-art of acoustic emission monitoring

A copious number of publications report research on the topic of damage detection and characterization in composite materials[19,20], but most of the materials studied are high quality aerospace materials, Kevlar and carbon-fiber reinforced polymer (CFRP). However, WTBs are a much lower cost structure containing glass-fiber reinforced polymer (GFRP), resin, and foam or wood. Due to the lower quality manufacturing requirements for WTBs compared to aerospace composites, a greater tolerance of quality variability occurs including resin variation and ply waviness. In addition to the different materials and manufacturing processes used, when compared to aerospace components, WTB designers employ thick sections of GFRP to increase strength. As shown in figure 2(b), the spar cap can be several cm thick, creating additional challenges for monitoring due to the change in elastic wave propagation.

AE monitoring has uses in laboratory blade fatigue studies, because it is able to effectively monitor damage formation[21,22]. Based on the location and the intensity of the recorded signals, AE events, the system provides good detection of failure zones before observable cracking begins. The primary method of tracking and detecting damage is using the Kaizer and Felicity effects. The Kaizer effect states that the number of AE events recorded increases with increased maximum applied load, and the Felicity effect occurs when the number of AE events increases before reaching the previous maximum load, signaling a structural change. In laboratory experiments, controlled loading and sensor placement on the exterior allow for optimal damage detection. Controlling the load provides an expected damage location, and the composite exterior provides uniform wave propagation. During real-time operation, WTBs experience various forms of loads and impact events, which can cause damage in any location requiring a need to monitor the entire WTB. Additionally during operation, the sensors monitor from the interior of the WTB where the structure, materials and resulting wave propagation are more complex.

Technical challenges faced with in-situ AE condition monitoring include the need for additional electronics, signal collection, and data analysis. Lightning strikes, responsible for 20% of WTB damage[23], can cause severe damage to an electronic system. Electronics are also susceptible to electromagnetic interference from the global electric circuit, static charge in the atmosphere, which can cause false alerts and increase noise[10]. Other technical issues of AE monitoring are the need for processing that can locate and quantify the damage. The complex structure of the WTB causes difficulties in collecting and interpreting the acoustic signals because of acoustic attenuation and scatter. Scattering can disrupt localization techniques, and attenuation reduces the signal amplitudes causing missed damage[23]. Table 1 shows experimental data by Sørensen et al[24]. on the signal range for PLB tests in different composites with different fabrication techniques. The high rate of signal attenuation in the composites used for WTBs causes signals to become undetectable after a propagation distance of about 600 mm, which limits the maximum spacing available between sensors, increasing the number of sensors needed.

Despite the challenges facing online health monitoring of WTBs, research is continuing to investigate the issue. McGugan et al. examined the ability of AE to detect damage in composite sandwich structures and applied the research to WTBs[25]. They discovered a correlation between the number of events, number of counts, and energy level and the level of damage that occurred in the WTB. Recent work by Papasalouros et al. is investigating AE monitoring of WTBs in operation[8]. Eight

piezoelectric sensors, mounted in the interior, monitored a 48m WTB. Three sensors attached to the root, two to the shear web, and the remaining three attached to the interior near the trailing edge. The system collected data for six months and did not detect any significant damage. The accumulated data correlated well with the loads and wind speeds experienced by the WTB. Another group researching AE monitoring of WTB is from IZFP Dresden. They outlined the potential and constraints of a system that contained 64 sensors with optical fiber power source and cables[26]. The number of required sensors is based on an estimated detectable range of approximately 1m. Bouzid et al. are researching the combination of wireless sensor networks with AE, specifically with respect to the use of low sampling rates[27]. Further overviews of WTB composites and structural health monitoring methods are available[28].

Table 1. Range for PLB test detection limit for 10 layer thick composite material[24].

	All Data	Hand Lay up fabrication	Injection Fabrication
Pure Resin	350-375 mm	350 mm	375 mm
Stress wave path parallel to reinforcing fibers	425 – 600 mm	425 – 600 mm	475 – 525 mm
Stress wave path transverse to reinforcing fibers	275 – 475 mm	350 – 400 mm	275 – 475 mm

3. THEORY

3.1 Waves in plates

Depending on the structure of the blade, the elastic wave will travel in different forms and modes. A wave propagates freely as a bulk wave if the medium is representatively infinite, which means the wavelength of the propagating wave is small with respect to the thickness of the medium. When the wavelength is not small with respect to the thickness, a finite medium, the waves propagate as guided waves. In a semi-infinite medium, Rayleigh waves will form along the surface and penetrate approximately 1.5 to 2 wavelengths below the surface. Another type of guided wave is the Stonely wave, which exists when two joined materials have a similar speed of sound. The waves will propagate along the interface only in the absence of flaws. The most common form of guided wave in finite structures is the Lamb wave. Lamb waves develop in relatively thin and narrow materials (defined in terms of wavelength) after a short time when the reflection and superposition causes the waves to form a wave packet[29].

Lamb first described wave motion in a plate with a theory that would assume his name[30]. Lamb wave theory describes waves spanning the thickness of the plate and having measurable interactions with both surfaces. The two primary wave modes, which exist in plates under these conditions, are extensional and flexural. Extensional waves have particle displacement in the same plane as the wave motion direction, and flexural waves have particle displacement in the plane normal to the direction of motion. Equations 1 and 2 express the extensional and flexural waveforms, respectively.

$$\frac{\tan(\beta_1 h)}{\tanh(\alpha_1 h)} = -\frac{4\alpha\beta k^2}{(k^2-\beta^2)^2} \tag{1}$$

$$\frac{\tan(\beta_1 h)}{\tanh(\alpha_1 h)} = -\frac{(k^2-\beta^2)^2}{4\alpha\beta k^2} \tag{2}$$

Where $\alpha^2 = \frac{\omega^2}{c_1^2} - k^2$, $\beta^2 = \frac{\omega^2}{c_2^2} - k^2$, and $k = \frac{\omega}{c_p}$, c_1 and c_2 represent the longitudinal and shear velocities, respectively, and c_p is the Lamb wave phase velocity in the plate.

Attenuation is the reduction of the amplitude of a wave as it propagates. The primary causes of attenuation are geometric spreading, thermal conversion, scattering, and absorption. Other causes are interface interaction, which is the loss due to energy leaving the plate into another material, and dispersion, which is the separation of the wave into different modes due to phase velocity differences. Geometric spreading is primarily the cause of attenuation in the near-field, but in far-field, scattering, absorption, and thermal conversion are the main causes. The basic equation for attenuation is an exponential.

$$E = E_o e^{-\alpha x} \tag{3}$$

Equation 3 is a simplification of the complex interaction between the medium and the wave energy. 'E' represents the energy at a distance 'x' from the source with an initial source energy of 'E_o', and attenuation coefficient of 'α'. In composite materials, attenuation is a critical issue due to heterogeneity and anisotropy. Both material properties play a role in the signal reduction, and analysis of the material's attenuation will provide a separate attenuation coefficient for each parameter. The geometry and internal structure may cause the attenuation coefficients to contain heterogeneity. Accounting for the materials contribution yields the following equations[16]:

$$E = E_o \left[1/x\right] e^{-2\alpha x} \tag{4}$$

$$P = P_o \left[1/\sqrt{x}\right] e^{-\alpha x} \tag{5}$$

Equation 4 and 5 represents the attenuation equation, where "E" is the energy of the waveform, and "P" is the amplitude at a specified frequency and the subscript '0' refers to the initial state. Energy relates to amplitude by $E = \int P^2 dt$.

As the wave travels, the different modes separate and each takes a portion of the total wave energy causing an overall decrease in the wave's amplitude. Highly dispersive materials will cause wave separation into numerous modes resulting in rapid attenuation in peak amplitudes. The dispersion curve can be calculated for both the symmetric and asymmetric modes using equations 6 and 7[31].

$$\frac{\tan(qh)}{q} + \frac{4k^2 p * \tan(ph)}{(q^2-k^2)^2} = 0 \tag{6}$$

$$\mathrm{q} * \tan(qh) + \frac{(q^2-k^2)^2 * \tan(ph)}{4k^2 p} = 0 \tag{7}$$

Iteratively evaluating equations 6 and 7 with different phase velocities and a specified frequency-thickness product, leads to the calculation of the dispersion curves.

Commercial codes are now available which can be used to determine dispersion curves. The Vallen software[32] requires inputs for the P-wave, S-wave, and material thickness. The aluminum used was Al 7075-T6 with the properties listed in table 3. Equations 8(a,b) determined the P-wave and S-wave speeds, respectively. To determine the dispersion curve for the composite material the P-wave speed and S-wave speed were calculated in the same way as for the aluminum, except the composite uses the specific modulus of elasticity and Poisson's Ratio for the direction of the fibers to determine the wave speed in the direction of the fibers.

$$c_p = \sqrt{\frac{E(1-\upsilon)}{\rho(1+\nu)(1-2\nu)}};\ c_S = \sqrt{\frac{E}{2\rho(1+\nu)}} \tag{8 (a, b)}$$

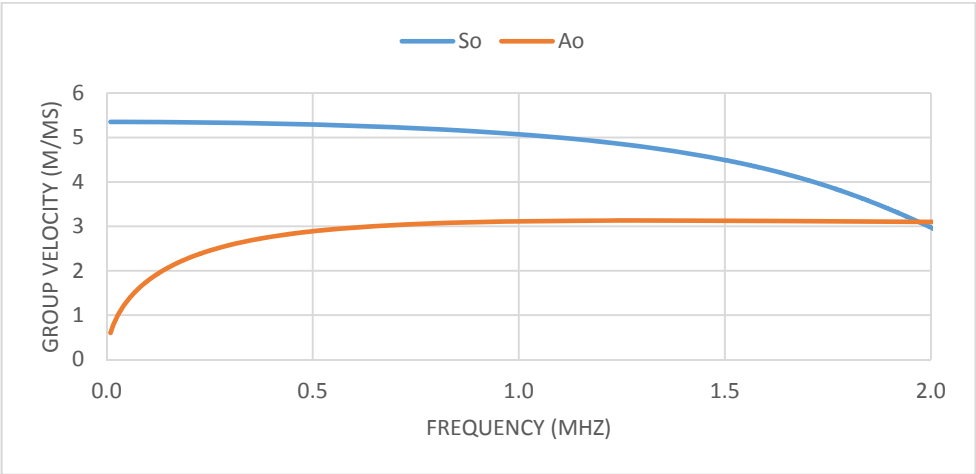

Figure 5. Dispersion curve for a 1mm thick aluminum plate generated from software[32]. Lower velocity is the $A_{0\ mode}$, and higher velocity is $S_{0\ mode}$.

The use of classical plate theory (CPT) enables the determination of the flexural and extensional mode velocities in isotropic materials as shown in figure 5, which shows the dispersion curve for a 1mm thick aluminum plate. The extensional wave speed is dispersion-less in the calculations for isotropic plates. The combination of CPT, exact elasticity, and laminate plate theory combine to form basic velocity estimations in laminate plates.

$$c_e = \sqrt{\frac{E}{(1-\nu^2)\rho}} \tag{9}$$

For the calculation of extensional velocity, c_e, E is the modulus of elasticity; ν is Poisson's Ratio; ρ is the density. The flexural mode contains dispersion and as such, it contains a frequency, w, and thickness, h, component.

$$c_f = \left[\frac{Eh^2}{12(1-\nu^2)\rho}\right]^{\frac{1}{4}}\sqrt{w} \tag{10}$$

The extensional velocity in laminates is also dispersion-less, and the flexural velocity depends on the frequency.

$$c_e = \sqrt{\frac{A_{11}}{\rho h}} \tag{11}$$

A_{11} is the in-plane laminate stiffness, and in the equation below, D_{11} is the bending stiffness.

$$c_f = \left[\frac{D_{11}}{\rho h}\right]^{\frac{1}{4}}\sqrt{w} \tag{12}$$

3.2 Wavelet transforms

A method for determining dispersion curves from time domain waveforms is the use of wavelet transforms[33], specifically the Gabor Wavelet Transform[34]. The transform converts a signal into a frequency-time spectrum, which allows for modal and frequency analysis of acoustic signals. A wavelet transform builds on the concept of the Fourier transform, which transforms a signal into the frequency domain. Short-time Fourier transforms or windowed Fourier transforms (WFT) multiply the signal by a short window function centered on a specific time and take the Fourier transform of the product. The Gabor transform, named after Dennis Gabor[35], applies a Gaussian window function. Additionally, the Gabor transform uses a constant width window function based on the lowest frequency of the signal, regardless of whether the window contains high or low frequencies.

The wavelet transform is an extension of the WFT and applies to continuous or discrete signals. The key difference between the WFT and the wavelet transform is that the window function adjusts with frequency when using a wavelet transform whereas it is constant in a WFT. The spectral width broadens with higher frequencies and narrows with lower frequencies, yielding better resolution for the lower frequencies. The wavelet transform also scales the amplitudes that result from the transform by implementing higher amplitudes for shorter time windows. The name "wavelet transform" arises from the use of short wavelength waves with limited duration for the basis function of the transform. The Gabor wavelet transform (GWT) is a specific wavelet transform defined by a specific basis function[36]. The GWT, used in this paper, has been shown to have good time-frequency resolution[34]. The continuous wavelet transform of a function f(t) is defined by equation 13.

$$(WT)(b,a) = \frac{1}{\sqrt{a}}\int_{-\infty}^{\infty} \Psi^*\left(\frac{t-b}{a}\right) f(t)\, dt \tag{13}$$

In equation 13, a > 0 and the * indicates a complex conjugate; $\Psi(t)$ is the basis function, or wavelet. Though a transform may use any basis function that satisfies the admissibility equation, the GWT uses the function in equation 14.

$$\Psi(t) = \frac{1}{\sqrt[4]{\pi}}\sqrt{\frac{\omega_p}{\gamma}}\; exp\left[\frac{-t^2}{2}\left(\frac{\omega_p}{\gamma}\right)^2 + i\omega_p t\right] \tag{14}$$

The Fourier transform of $\Psi(t)$ is $\widehat{\Psi}(t)$.

$$\widehat{\Psi}(\omega) = \frac{\sqrt{2\pi}}{\sqrt[4]{\pi}}\sqrt{\frac{\gamma}{\omega_p}}\, exp\left[\frac{-\left(\frac{\gamma}{\omega_p}\right)^2}{2}\left(\omega-\omega_p\right)^2\right] \tag{15}$$

In equations 14 and 15, $\omega_p = \frac{\sqrt{2}\pi}{\Delta t}$ and is the central frequency; $\gamma = \pi\sqrt{\frac{2}{\ln(2)}}$ is a constant that must satisfies the admisibility condition, because wavelets must satisfy the orthonormality condition. The initial function $\Psi\left(\frac{t-b}{a}\right)$ is centered on t = b

and its Fourier transform is centered on $\omega = \omega_p/a$, which results in the wavelet transform representing the time-frequency component of f(t) around t=b and $\omega = \omega_p/a$.

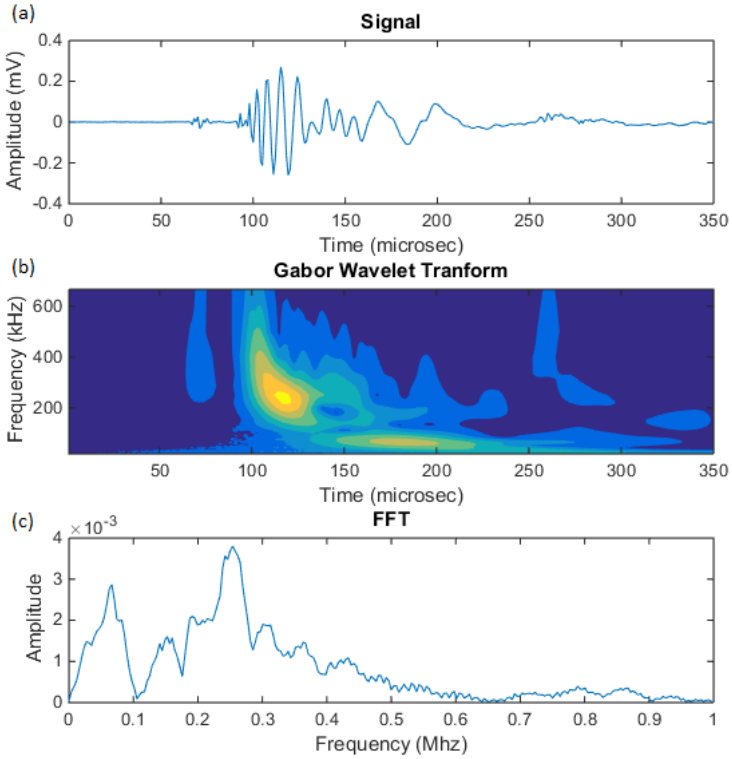

Figure 6. An example of (a) a time signal resulting from a lead pencil break measured at 5 cm range. (b) The Gabor wavelet transform for the signal in (a), and (c) the Fourier transform of the signal in (a) showing the peak frequencies.

Research has been done to use the wavelet tranform to differentiate modes in a signal[37] and extract additional data[18]. Figure 6 shows an example of the GWT for a PLB signal measured at 5 cm range. The transform allows for identification of the extensional and flexural waves and visually shows the arrival time of each frequency peak. The extensional wave begins after 50 microseconds, and the flexural wave begins before 100 microseconds in both the signal and the wavelet plots. The contour plot represent the intensity of the frequency at the specific time, with lighter shades representing higher amplitudes. The frequency intensities of the wavelet transform shown in figure 6(b) correspond to the high amplitude frequencies shown in by the Fourier transform in figure 6(c). The Fourier transform reveals a peak frequency of approximately 250 kHz, which coincides with the peak wave intensity in the wavelet transform at approximately 250 kHz and 45 microseconds. The wavelet transform reveals the different wave modes, frequencies, and frequency intensities in the time domain.

4. EXPERIMENT

4.1 Experimental system

The experiments used a Digital Wave data acquisition system (DAQ), Digital Wave preamplifier, and multiple broadband piezoelectric sensors. The Digital Wave B1025 sensors have a bandwidth from, 1 kHz to 1.5 MHz, a peak frequency of 250 kHz, and a 6.35 mm diameter. A petroleum gel (Vaseline) was used as the couplant between the material and the AE sensors. The preamplifier (PA-20) supplies 20dB of gain to the signal between the sensor and the DAQ. The DAQ, FM-1, implements a secondary preamplifier, signal gain, and filter to process the data before digitizing the signal. Employing the units low pass (LP) and high pass (HP) filter reduced noise and improved signal clarity (S:N). After the DAQ collected the data, it was digitized and sent to the computer for post processing. Digital Wave WaveExplorer and Matlab software were used to analyze the received signals in the time and frequency domains.

To derive the values needed, separate tests were executed on each of the plates. As shown in figure 7, all sensors were placed along the center of the plates to avoid edge effects. Table 2 shows the layout for the two tests performed on each of the plates. The 'x' in parenthesis represents the location of the PLB. Test 1 was the layout used for the extensional tests, and Test 2 was the layout used for the flexural tests. Figure 7 shows the setup used in Test 1 for each of the examined plates. The sensor spacing increases with distance from the source to track the rate of change of attenuation and wave speeds.

Table 2. Sensor Layout for Aluminum and Composite Test where (x) represents lead break location (mm).

	Composite	Aluminum
Test 1	0(x), 50, 100, 150, 200, 300, 400, 500, 600	0(x), 100, 200, 300, 400, 500, 600, 700, 800
Test 2	30(x), 40, 50	200, 400, 600(x), 800, 1000

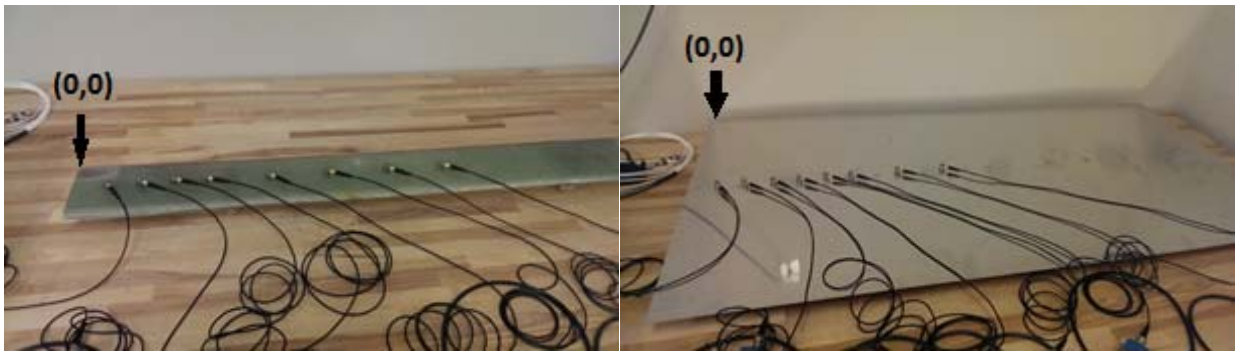

(a) (b)

Figure 7. The test setup for (a) the GFRP and (b) the aluminum plate under Test 1 condition. Sensor spacing described in table 2.

Table 3 lists the properties of the two materials used in the experiments, Aluminum and GFRP. Based on the aluminum type, materials properties were obtained from the MatWeb[38] database, and colleagues at Iowa State University, who manufactured the composite, provided the stiffness matrix for the GFRP. The Young's Modulus and Poisson's ratio were determined for the direction of the fibers using the equations for composite structural mechanics. The material properties were used in equations 8(a,b) to provide the longitudinal and shear wave speeds. The width of the GFRP was able to be less than the aluminum width due to a slower longitudinal wave speed and higher attenuation rate, which reduce edge effects.

Table 3. Material Properties for the aluminum[38] and glass-fiber reinforced polymer (GFRP).

	Aluminum 7075-T6	GFRP Test
Density	2810 $\frac{kg}{m^3}$	1580 $\frac{kg}{m^3}$
Young's Modulus	71.7 GPa	43.3 GPa
Poisson's Ratio	0.33	0.21
Longitudinal Wave Speed	6150 m/s	5490 m/s
Shear Wave Speed	3097 m/s	3390 m/s
Size	1215x608x1 mm	1000x40x10 mm

5. RESULTS

5.1 Aluminum analysis

The initial experiments were performed to determine the wave speeds of the extensional and flexural modes in the aluminum. The extensional wave velocity for frequencies below 500 kHz is relatively constant in plates, as seen in the dispersion curve for a 1 mm thick aluminum plate shown in figure 5. Table 4 shows the theoretical wave speeds, where the S_o speed is calculated from equation 9 and the A_o speed is extracted from the dispersion curve in figure 5. Equation 9 provides a good approximation to the extensional wave speed, because the extensional component is almost non-dispersive under these conditions. Because of the frequency dependence of the flexural wave, the theoretical speed is taken from the dispersion curve.

Equation 16 shows the conversion of milli-volts, taken from the measured signals, to decibels, used in attenuation analysis. The rate of attenuation is based on the change in the peak amplitude and the distance from the source. Each sensor provides a peak amplitude measurement, 'A', with the first sensor amplitude being the reference amplitude, 'A_{ref}'. Multiplying the decibel level by the square root of the distance between the sensor and the reference point accounts for beam spreading.

$$dB = 20 * \log\left(\frac{A_{ref}}{A}\right) * \sqrt{d} \qquad (16)$$

The first test (Test 1 of table 2) determined the extensional wave speed and attenuation for waves from a PLB on the side of the aluminum plate and the signal measured with sensors spaced 100mm apart. As described in section 2.2, the in-plane displacement causes high amplitude extensional waves. Tracking the time of flight of the first recorded wave produced the wave speed and the attenuation of the extensional, S_o, mode. The first row of table 4 shows the comparison of the experimental values to those calculated from CPT and those given in the literature[39]. The reference case examined a 3.1mm thick aluminum plate, which may contribute to the lower attenuation. The theoretical value is determined from CPT for extensional modes (Equation 9).

Table 4. Comparison of experimental results (Exp.) to reference case (39) and theoretical values.

	Ref. Attenuation[39]	Exp. Attenuation	Theoretical Speed	Exp. Speed
S_o Mode	5-12 dB/m	9 dB/m (+/- 7)	5350 m/s	5380 m/s (+/- 130)
A_o Mode	4-10 dB/m	25 dB/m (+/- 2)	2280 m/s	2130 m/s (+/- 100)

Test 2 used the second layout from Table 2, and the PLB was performed on the surface near the center of the plate. The sensors were placed along the center of the plate with the source placed very near the center of the plate to reduce and avoid edge effects. The out-of-plane displacement, described in section 2.2, excited high amplitude flexural waves and low amplitude extensional waves. Detecting the peak amplitude of the waveform provided the data needed to determine the flexural wave speed and attenuation. Tracking the maximum amplitude provided varying wave speeds, but using the GWT allowed the monitoring of a specific frequency. Using 200 kHz the wave speed was determinable and seen to be comparable to the wave speed shown in table 4, which is from the calculated dispersion curve in figure 5.

The attenuation was found by recording the peak amplitude in the two test cases, out-of-plane and in-plane. The peak amplitude in the out-of-plane test provided the data for attenuation of the flexural mode, and the peak amplitude in the in-plane mode provided the data for attenuation of the flexural mode. The signal amplitude in mV was converted to dB using equation 16, where the reference amplitude was the first recorded maximum signal.

5.2 Composite analysis

The experiment was repeated on GFRP material and the wave speed and attenuation were determined for the extensional and flexural modes. The theoretical extensional and flexural wave velocities were calculated from Equations 11 and 12, respectively. The extensional component compared well with the theoretical value, though it was found to be slower than the theory. The experimental flexural wave velocity is frequency dependent and corresponded to the theoretical velocity at 32 kHz, despite the experimental frequencies being between 100 and 200 kHz. The discrepancy between the two frequencies is discussed in section 5.3.

Table 5 shows the data for attenuation for the GFRP as well as the wave speeds. The attenuation, in the direction of the fibers, was determined in the same way as it was for the aluminum and was compared to a CFRP reference case. Because of the material structure, it is expected that the GFRP will have a higher rate of attenuation than CFRP.

Table 5. Comparison of experimental results (Exp.) to reference (Ref.) and theoretical values.

	Ref.[39] Attenuation	Exp. Attenuation	Theoretical Speed	Exp. Speed
S_o Mode	4-5 dB/m	23 dB/m (+/-2)	5330 m/s	5070 m/s (+/- 130)
A_o Mode	53-60 dB/m	28 dB/m (+/-2)	1730 m/s	1630 m/s (+/- 70)

5.3 Waveform analysis

A second objective was to examine the use of wave transforms for identifying the wave modes in the aluminum and the GFRP. The Gabor wavelet transform (GWT) converts the signal from the time domain into a 3D representation of frequency, time, and transform coefficient. The transform coefficient corresponds to frequency intensity at specific points in time. The transform allows the frequency intensities to be seen in the time domain providing the ability to determine the frequency specific wave velocities based on the arrival time. Combining the phase velocities and frequencies allows the reconstruction of the dispersion curve, as seen in figures 8, 9, and 10.

The arrival time of the peak amplitude for each frequency is determinable using the GWT. Figure 8 shows the comparison of group velocities determined from the transform and the theoretical values determined using the Vallen software and equations 8(a) and 8(b) for the longitudinal and shear velocities.

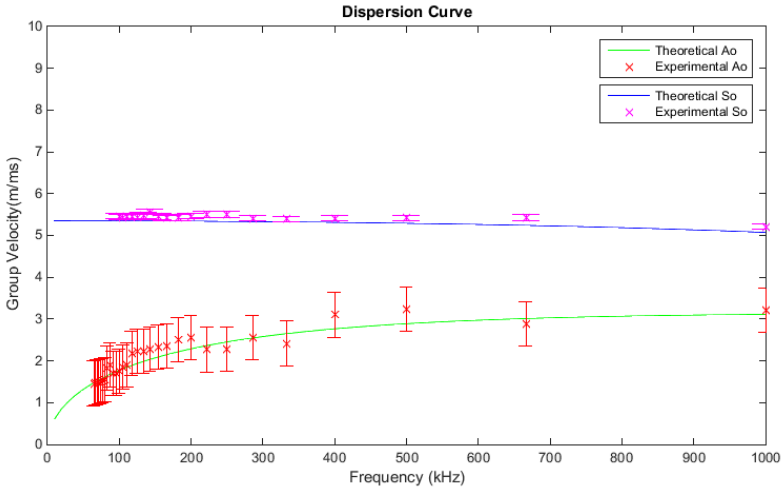

Figure 8. Dispersion curve for 1mm thick aluminum plate. The 'x' with error bars represent the experimental values whereas the straight lines are the theoretical values from CPT. The higher velocity component is the extensional, S_o, component and the lower speed component is the flexural, A_o, mode.

The GWT was applied to the GFRP signals to discern the dispersion curves for the composite material. Figure 9 shows the extensional dispersion curve for the GFRP plate. The theoretical curve is calculated using equations 8(a) and 8(b) to determine the longitudinal and shear wave speeds. The modulus of elasticity and Poisson's Ratio were taken in for the direction of the fibers. The values were then applied to the Vallen software to calculate the curve.

Figure 10 shows two theoretical dispersion curves and the experimental values for the flexural wave. The flexural dispersion curve determined from equations 8(a) and 8(b) did not apply to the flexural component of the composite plate. Implementing the equation for shear velocity from Mindlin theory provides better agreement between theory and experimental data[40].

$$v_s = \sqrt{\frac{G}{\rho}} \tag{17}$$

In equation 17, v_s is the shear velocity; G is the bulk modulus; ρ is the density. CPT does not provide a good representation of the flexural mode because it assumes the effects of shear deformation and rotatory inertia are negligible[41]. Mindlin plate theory provides a much more agreeable result.

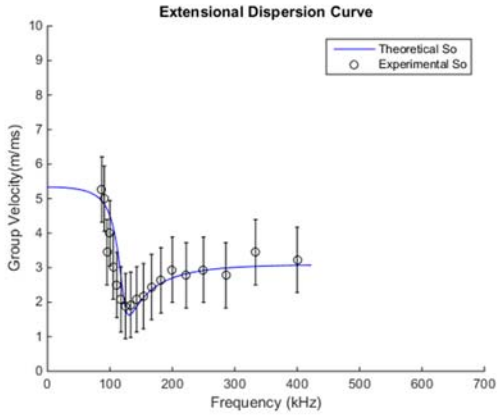

Figure 9. Extensional dispersion curve for 10mm thick composite GFRP plate. The 'o' with error bars represent the experimental values and the solid line represents the theoretical curve calculated from CPT.

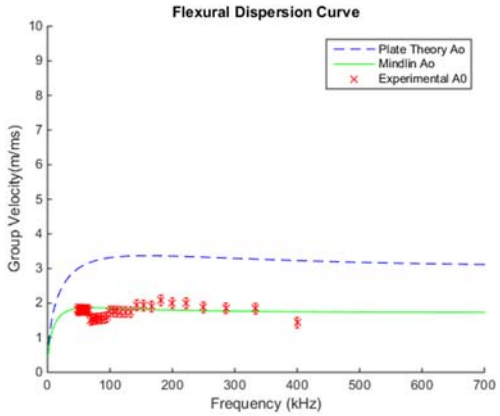

Figure 10. Flexural wave dispersion curve for 10mm thick composite GFRP. The 'x' represents the experimental values; the solid line represents the theoretical line calculated from Mindlin theory, and the dashed line represents the theoretical curve from classic plate theory.

6. SUMMARY OF RESULTS

The purpose of this paper was to provide foundational data for acoustic emission monitoring of GFRP, specifically for the guidance of future AE research with the application to OSHM of WTBs. Piezoelectric sensors attached to a data acquisition system detected elastic waves emitted from a pencil-lead break (PLB) source. The PLB source occurred on both the top and on the side of the plate to excite the two different wave modes. Using peak-amplitude tracking the group velocity and attenuation rates for the flexural and extensional wave modes were determined. The decrease in amplitude from sensor to sensor provided the attenuation rates. The Gabor wavelet transform enabled the determination of frequency specific wave speeds leading to the creation of the dispersion curves. Classic Plate Theory (CPT) was the foundation for calculating the theoretical wave speeds and dispersion curves. Aluminum plate tests verified the system and methods used by finding good agreement between the theoretical and experimental values of the wave speeds. The attenuation varied from the reference case, but the increase in flexural attenuation over the extensional case is expected.

Examining the GFRP included testing for the group velocities and rate of attenuation and creating the dispersion curves with the use of the GWT. The attenuation in the GFRP is higher than the attenuation in aluminum and CFRP due to the materials and manufacturing process used for GFRP. The use of the GWT enabled the construction of the dispersion curves for both modes of GFRP. The dispersion curve of the flexural mode of the composite material did not match the CPT curve. An alternate model using Mindlin plate theory, which includes the effects of shear deformation and rotatory inertia providing much better agreement between theory and experimental data.

The flexural wave mode is strongest in the out-of-plane orientation, and the extensional mode is strongest in the in-plane orientation. The use of the ratio of flexural and extensional wave amplitudes can provide information concerning the damage type and location. The results shown here reveal the potential to monitor the GFRP material used in WTB applications, specifically with respect to sensor spacing and mode identification with the GWT. The higher rate of attenuation for the flexural component sets the limits for the maximum separation of sensors.

7. CONCLUSION

In conclusion, the group velocities of lamb waves in GFRP composite material were analyzed. Based on PLB tests, sensors with a bandwidth in the frequency range between 50 and 300 kHz are sufficient to detect both the primary flexural and extensional wave modes. The dispersion curves were analyzed and compared to CPT using Vallen software. The extensional dispersion curve closely followed the modeled data, but the flexural wave mode required the implementation of Mindlin plate theory. Based on previous and the current work it can be preliminarily shown that sensor spacing for complete coverage should be limited to 1 meter due to the rate of attenuation of both the flexural and extensional wave modes.

ACKNOWLEDGMENTS

The research reported in the paper has been supported by the National Science Foundation Integrative Graduate Education and Research Traineeship (IGERT) award in Wind Energy Science, Engineering, and Policy (WESEP), at Iowa State University and work was performed at the Center for NDE, Iowa State University an NSF IU CRC.

REFERENCES

[1] "Top 5 Wind Energy Claims," GCube Insurance Services, Inc. (2013).
[2] Wiser, R. and Bolinger, M., "2013 Wind technologies market report," U.S. Department of Energy: Energy Efficiency &Renewable Energy, Berkeley, LBLN-6809E, (2014).
[3] Crabtree, C., Zappalà, D., and Tavner, P., "Survey of commercially available condition monitoring systems for wind turbines," SUPERGEN WIND, Durham University, May 05, (2014).
[4] Besnard, F., Nilsson, J. and Bertling, L., "On the economic benefits of using condition monitoring system for maintenance management of wind power systems," Proc. 2010 IEEE 11th International Conference on Probabilistic Methods Applied to Power Systems, Singapore, 14-17 (2010).
[5] Pérez, J., Asensio, E. and Márquez, F., "Economic viability analytics for wind energy maintenance management," [Advanced Business Analytics], Springer International Publishing, Switzerland, 39-54 (2015).
[6] May, A., McMillan, D. and Thöns, S., "Economic analysis of condition monitoring systems for offshore wind turbine sub-systems," Proc. EWEA, (2014).
[7] Beattie, A. G., "Acoustic emission monitoring of a wind turbine blade during a fatigue test," Proc. 35th Aerospace Science Meeting, Reno, NV, Jan. (1997).
[8] Papasalouros, D., Tsopelas, N., Anastasopoulos, A., Kourousis, D., Lekou, D. J. and Mouzakis, F., "Acoustic emission monitoring of composite blade of NM48/750 NEG-MICON wind turbine," Journal of Acoustic Emission 31, 36-49 (2013).
[9] Barr, A., "Blade market and technology trends update," MAKE Consulting, Wind Turbine Blade Workshop Presentation (2014).
[10] Rumsey, M., "An evaluation of sensing technologies in a wind turbine blade: some issues, challenges and lessons learned," (Eds. K. Farinholt and S. Griffin), Proc. SPIE, 7979, Industrial and Commercial Applications of Smart Structures Technologies. San Diego, California, 79790G-15, (2011).
[11] Nolet, S., "Composite wind blade engineering and manufacturing," TPI Composites, Inc., (2011).
[12] Richardson, M. O. W. and Wisheart, M.J., "Review of low-velocity impact properties of composite materials," Composites Part A 27A, 1123-1131 (1996).
[13] Gorman, M., "Plate wave acoustic emission," Journal of Acoustic Society of America 90(1), 358-364 (1991).
[14] Hsu, N. N. and Beckenridge, F. R., "Characterization and calibration of acoustic emission sensor," Materials Evaluation 39(1), 60-68 (1981).
[15] Hsu, N., "Acoustic emissions simulator," U.S. Patent 4018084 A, April 19, 1977.

[16] Sause, M., "Investigation of pencil-lead breaks as acoustic emission sources," Journal of Acoustic Emission 29, 184-196 (2011).
[17] "Standard guide for determining the reproducibility of acoustic emission sensor response," ASTM Standard E970-10, (2010).
[18] Kishimoto, K., Inoue, H., Hamada, M. and Shibuya, T., "Time frequency analysis of dispersive waves by means of wavelet transform," Journal of Applied Mechanics 62, 841–846 (1995).
[19] Ono, K. and Gallego, A., "Research and applications of acoustic emission on advanced composites," Proceedings 30th European Conference on Acoustic Emission 2012 (Eds. A Gallego and K Ono) ISBN 978-84-615-9941-7, Granada, Spain, 1-44, September 12-15 (2012).
[20] Holford, K. M., "Acoustic emission in structural health monitoring," Key Engineering Materials 413-414, 15-28 (2009).
[21] Dutton, A. G., Blanch, M., Vionis, P., Kolovos, V., van Delft, D. R. V., Joosse, P., Anastassopoulos, A., Kouroussis, D., Kossivas, T., ter Laak, J., Philippidis, T.P. Kolaxis, Y. G., Fernando, G., Zheng, G., Liu, T. and Proust, A., "Acoustic emission monitoring from wind turbine blades undergoing static and dynamic fatigue testing," British Journal of NDT Insight 42(12), 805-808, December (2000).
[22] Joosse, P. A., Blanch, M. J., Dutton, A. G., Kouroussis, D. A., Philippidis, T. P. and Vionis, P. S., "Acoustic emission monitoring of small wind turbine blades," Journal of Solar Energy Engineering 124(4), 446-454 (2002).
[23] Lee, J., Shin, H., Chia, C. C., Dhital, D., Yoon, D. and Huh, Y., "Long distance laser ultrasonic propagation imaging system for damage visualization," Optics and Lasers in Engineering 49(12), 1361-1371 (2011).
[24] Sørensen, B., Lading, L., Sendrup, P., McGugan, M., Debel, C., Kristensen, O., Larsen, G., Hansen, A., Rheinlander, J., Rusborg, J. and Vestergaard, J., "Fundamentals for remote structural health monitoring of wind turbine blades – a preproject," Risø-R-1336(EN) Report, Risø National Laboratory, Rokilde (2002).
[25] McGugan, M., Sørensen, B. F., Østergaard, R. and Bech, T., "Detecting and identifying damage in sandwich polymer composite by using acoustic emission," Risø-R-1580(EN) (2006).
[26] Schubert, L., Schulze, E., Frankenstein, B., Fischer, D., Weihnacht, B. and Rieske, R., "Monitoring system for windmill rotorblades based on optical connections," Proc. SPIE 7982, 1-8 (2011).
[27] Bouzid, O., Tian, G.Y., Cumanan, K. and Moore, D., "Structural health monitoring of wind turbine blades: acoustic source localization using wireless sensor networks," Journal of Sensors, Article ID 139695, in press (2015).
[28] Yang, W., "Testing and condition monitoring of composite wind turbine blades," Recent Advances in Composite Materials for Wind Turbine Blades, (Ed. B. Attaf), The World Academic Publishing Co. Ltd., 147-169 (2013).
[29] Aljets, D., "Acoustic emission source location in composite aircraft structures using modal analysis," Ph. D. Dissertation, University of Glamorgan/Prifysgol Morgannwg (2011).
[30] Lamb, H., "On waves in an elastic plate," Royal Society of London, Series A, Containing Papers of a Mathematical and Physical Character, The Royal Society 93(648), 114-128 (1917).
[31] Rose, J., [Ultrasonic guided waves in solid media], Cambridge University Press, New York City (2014).
[32] Vallen, J., "Vallen Dispersion Software, Version R2005.1121," Vallen-Systeme GmbH, Munich Germany (2005).
[33] Carmona, R., Hwang, H. L. and Torres, B., [Practical time-frequency analysis], London: Academic Press, (1998).
[34] Gabor, D., "Theory of communication. Part 1: The analysis of information," Journal of the Institution of Electrical Engineers-Part III: Radio and Communication Engineering 93(26), 429-441 (1946).
[35] Suzuki, H., Kinjo, T., Hayashi, Y., Takemoto, M. and Ono, K., "Wavelet transform of acoustic emission signals," Journal of Acoustic Emission 14(2), 69-84 (1996).
[36] Chui, C.K., [An introduction to wavelets], Academic Press, San Diego, CA (1992).
[37] Wang, L., "Elastic wave propagation in composites and least-squares damage localization technique," Ph. D. Dissertation, North Carolina State University (2004).
[38] MatWeb, "ASM Aerospace Specification Metals Inc.," (2014) http://asm.matweb.com/search/SpecificMaterial.asp?bassnum=MA7075T6.
[39] Ono, K. and Gallego, A., "Attenuation of lamb waves in CFRP plates," Journal of Acoustic Emission 30, 109-123, (2012).
[40] Stephen, N. G., "Mindlin plate theory: best shear coefficient and higher spectra validity," Journal of Sound and Vibration 202(4), 539-553 (1997).
[41] Prosser, W. H. and Gorman, M. R., "Plate mode velocities in graphite/epoxy plates," Journal of Acoustical Society of America 96(Part I), 902-907 (1994).